The Association Between Cloud Droplet Number Over the Summer Southern Ocean and Air Mass History.

Gerald G. Mace[1], Sally Benson[1], Elizabeth Sterner[1], Alain Protat[2,3], Ruhi Humphries[3,4], A. Gannet Hallar[1]

1. Department of Atmospheric Sciences, University of Utah
2. Bureau of Meteorology, Melbourne, Australia
3. Australian Antarctic Program Partnership, Hobart, Tasmania, Australia
4. CSIRO Environment, Melbourne, Australia

Abstract: The cloud properties and governing processes in Southern Ocean marine boundary layer clouds have emerged as a central issue in understanding the Earth's climate sensitivity. While the simulated cloud feedbacks in Southern Ocean clouds have evolved in the most recent climate model intercomparison, the background properties of simulated summertime clouds in the Southern Ocean are not consistent with measurements due to known biases in simulating cloud condensation nuclei concentrations. This paper presents several case studies collected during the Capricorn 2 and Marcus campaigns held aboard Australian research vessels in the Austral Summer of 2018. Combining the surface-observed cases with MODIS data along forward and backward air mass trajectories, we demonstrate the evolution of cloud properties with time. These cases are consistent with multi-year statistics showing that long trajectories of air masses over the Antarctic ice sheet are critical to creating high droplet number clouds in the high latitude summer Southern Ocean. We speculate that secondary aerosol production via the oxidation of biogenically derived aerosol precursor gasses over the high actinic flux region of the high latitude ice sheets is fundamental to maintaining relatively high droplet numbers in Southern Ocean clouds during Summer.

Plain Language Summary: The amount of warming the Earth will experience because of increasing carbon dioxide levels in the atmosphere is sensitive to the properties of clouds that occur over the Southern Ocean. The atmosphere over the circumpolar Southern Ocean is poorly understood and presents significant challenges to climate models. Here we document the properties of the ubiquitous Southern Ocean low-level clouds that exert a strong influence on the albedo of this region. We find that high cloud droplet number concentrations are associated with air masses that have taken paths over the high-altitude ice sheets. The chemistry of the aerosol on which the cloud droplets form suggests that newly formed aerosols that have condensed from gasses emitted by phytoplankton in the highly productive waters near Antarctica are an important component of the cloud properties that must be correctly simulated in models.

Main Point 1: High cloud droplet number concentrations are associated with air masses that have recently passed over continental Antarctica.

Main Point 2: Cloud droplet number concentrations decrease with time as clouds evolve in over-water trajectories due to scavenging by precipitation.

Main Point 3: Katabatic flows bring high concentrations of cloud condensation nuclei to the marine boundary layer where they influence cloud properties.

1 Introduction

As one of the cloudiest regions on Earth, with cloud cover near 90% (Mace et al., 2009; Mace & Zhang, 2014), the high latitude Southern Ocean from roughly poleward of the Antarctic Circumpolar Current to the Antarctic Continent is a critical component of the Earth's climate system. In addition to fundamental oceanographic processes such as the uptake of atmospheric heat and carbon in the formation of the intermediate and deep-water masses (Armour et al., 2016; Morrison et al., 2016), the albedo of the extensive cloud cover, particularly in summer, induces significant controls on the column energy budget of the region and influences the Earth's climate (Zelinka et al., 2020; Gettelman et al., 2019).

The high cloud cover of the Southern Ocean is primarily due to extensive marine boundary layer (MBL) clouds, most of which are liquid phase and subfreezing (Bodas-Salcedo et

al., 2016). These clouds, while mostly nonprecipitating (Huang et al., 2016), generate both liquid- and ice-phase precipitation (Mace et al., 2021). Because precipitation exerts controls on cloud cover (Albrecht et al., 1989), precipitation in these clouds continues to be a topic of active research (Kang et al., 2022). However, cloud properties and the associated cloud albedo, as well as the precipitation processes, respond to a significant seasonal cycle in cloud condensation nuclei (CCN) that directly influence cloud droplet number concentration (N_d) (McCoy et al., 2015; Kruger and Grasl, 2011; Mace et al., 2023, 2021). Analyzing cloud properties derived from A-Train data, Mace and Avey (2017) find that the Summer N_d in the SO is approximately a factor of two higher in summer compared to winter. While this seasonal cycle in N_d is thought to be associated with seasonally higher CCN associated with due to secondary aerosol production derived from the oxidation of biogenically-derived precursor gasses such as dimethyl sulfide (DMS) (Lana et al., 2012), aerosol measurements collected during recent campaigns have not directly observed new particle formation events. However, robust circumstantial evidence suggests that new particle formation of sulfur-based particles with a volatility similar to sulfuric acid in the SO free troposphere is widespread and frequent (McCoy et al., 2021).

This hypothesis is consistent with prior studies suggesting that particle concentrations in the free troposphere in marine regions are controlled by sulfuric-acid-driven nucleation of nanoparticles resulting from the oxidation of oceanic dimethylsulfide transported upward. Downward transfer of these nanoparticles then supplies the marine boundary layer with CCN concentration. This mechanism of aerosol production has been observed (Clarke, 1993) and modeled (Russell et al., 1994; Raes, 1995) previously. Most recently, laboratory work on sulfuric acid nucleation and further growth have demonstrated that these processes can survive evaporation and even grow during these transport processes and temperature transitions (Tiszenkel et al., 2019)

Trajectory analyses also point to a source of CCN from airmasses emanating from the Antarctic continent (Humphries et al., 2016; Twohy et al., 2021; Simmons et al., 2021). Specifically, the Antarctic continent in summer has been identified as a potential source of sulfate aerosol in work dating back to the 1980's (Shaw, 1988). Presumably, air masses with high DMS and oxidants are lofted over the high albedo and mostly cloud-free ice sheets in synoptic scale ascent, where most ambient aerosols are removed by precipitation. New sulfate-containing aerosol particles nucleate and grow during the time spent over the ice sheets in the

cold free-troposphere. Katabatic flows then cause these newly formed aerosols to emerge into the marine boundary layer in the waters adjacent to the Antarctic continent (Simmons et al., 2021).

Using MODIS data, we recently showed that N_d in the East Antarctic sector of the SO exhibits strong latitudinal gradients during Summer, with the highest N_d in the waters immediately adjacent to the Antarctic Continent (Mace et al., 2023). These results agreed broadly with findings compiled from the Measurements of Aerosols, Radiation, and Clouds over the Southern Ocean (MARCUS) and the Clouds, Aerosols, Precipitation, Radiation, and atmospheric Composition over the Southern Ocean (CAPRICORN II) (McFarquhar et al., 2021) campaigns that collected data in this region during Summer 2018 (Mace et al., 2021). The latitudinal gradient in N_d is a curious feature of the SO region. It seems consistent with the idea that the highest CCN concentration is found immediately adjacent to the Antarctic continent. Cloud and precipitation processing of the aerosol then decrease N_d with distance away from the Antarctic coast. However, the CCN concentration and N_d remain mostly above sea salt aerosol concentration, suggesting a source of new particles mixing into the MBL from the free troposphere (McCoy et al., 2021). The extent to which the background CCN and N_d are maintained against cloud processing by mixing from the free troposphere, as suggested by Twohy et al. (2021) and McCoy et al. (2021), is unknown.

The processes that maintan N_d in the summer SO are crucial to understanding the Earth's climate sensitivity. In the most recent climate model intercomparison project (CMIP6; Eyring et al., 2016), the high latitude SO had significantly less negative cloud feedback than in CMIP5 and earlier model intercomparison studies. While this change in simulated cloud feedback was due partially to an observationally consistent decrease in ice-phase precipitation, the cloud feedback change occurred within a simulated background state in cloud properties that is unrealistic. As shown by McCoy et al. (2021), the CAM6 model consistently underpredicts, by approximately a factor of 2, the N_d in comparisons to collocated measurements during the Southern Ocean Cloud Radiation Aerosol Transport Experimental Study (SOCRATES) campaign (McFarquhar et al., 2021). McCoy et al., (2021) trace this bias to an insufficient DMS oxidation mechanism in the model among other issues. Since N_d and precipitation scale inversely in MBL clouds (Comstock et al., 2004), a correct simulation of N_d is a prerequisite to correctly predicting the precipitation

that is driving the negative feedback changes in CAM6 (Gettleman et al., 2019) poleward of about 50°S.

This paper examines three case studies collected in the Australian East Antarctic sector of the SO from the Summer of 2018 during the MARCUS and CAPRICORN II campaigns. Using a combination of surface-based cloud property diagnostics and aerosol in situ measurements, we examine MODIS-derived cloud properties along backward and forward trajectories. We show that clouds forming in air masses recently descended in Katabatic flows from the high-altitude Antarctic ice sheets have significantly higher N_d than the mean for that latitude. The N_d then decreases with time as the air masses pass over the open ocean. We then place these case studies within a larger context of MODIS data collected over 5 Austral Summers to show a consistent relationship between N_d and trajectories emanating from the Antarctic continental ice sheets.

2. Methods

In this study, we combine data from the MARCUS and CAPRICORN II ship-based campaigns with MODIS level 2 data products extracted from overpasses along backward and forward airmass trajectories centered on the ships. This combination of surface and satellite measurements linked by trajectory modeling allows us to exploit the synergy in the surface and satellite measurements. While polar-orbiting satellite measurements provide spatial context, they only provide a single snapshot in time and have only limited information on the cloud field. Surface-based measurements fill in the missing temporal element and add significant detail but are limited spatially. Using airmass trajectories derived from model output, we can combine the spatial information from MODIS with the much more detailed information from the surface to address the role of airmass history in governing cloud properties in the high-latitude Southern Ocean.

a. Ship Data

The CAPRICORN II voyage occurred from 11 January to 21 February 2018 between Hobart, Tasmania, and the East Antarctic coastal region. CAPRICORN II collected oceanographic data along transects between the 130°-150°E meridians by occupying some 88 stations from 6 to 24 hours where oceanographic data were collected, followed by movement to

148 the next station several tens of km distant. This approach was advantageous for atmospheric data
149 collection, allowing for longer periods of measurements at latitudes infrequently sampled by
150 voyages focusing on the highest latitudes. On the other hand, the DOE ARM-funded MARCUS
151 deployed instrumentation on the Aurora Australis that was conducting resupply of the Australian
152 Antarctic stations (McFarquhar et al., 2019). Since resupply was the primary objective of the
153 ship, the Aurora Australis made best time between Hobart and the Australian stations in 5
154 voyages starting in Hobart between November 2017 and March 2018. For a more thorough
155 description of these campaigns, see Mace et al. (2021) and McFarquhar et al. (2019, 2021). The
156 cloud and aerosol measurement instrumentation are described in detail in the supplemental
157 material of McFarquhar et al. (2021).
158 Cloud properties from the surface-based measurements are derived using a synergistic
159 approach described in Mace et al. (2021). Combining measurements from collocated and
160 vertically pointing W-Band radars, optical elastic lidars, and microwave radiometers (MWR) on
161 each ship, we derive N_d and cloud-top effective radius (r_e) of shallow cloud layers based in the
162 MBL. Our methodology allows for a liquid water path (LWP) constraint provided by the MWR
163 (Turner et al., 2016), and the radar and lidar are combined to constrain N_d and r_e given the LWP.
164 Constraints on N_d and r_e are possible by assuming that N_d is constant with height and the
165 observed liquid water path is distributed subadiabatically, knowing the cloud geometry. The
166 LWP uncertainty is 20% for LWP more than 100 g m^{-2}, scaling to 100% near the detection limit
167 of 20 g m^{-2} while the r_e and N_d retrievals have uncertainty of 30% and 100%, respectively.
168
169 b. Airmass Trajectories
170 We derive 120-hour airmass back and forward trajectories based on the ship location for
171 specific case studies centered on the time of a MODIS overpass. The trajectories are calculated
172 using the National Center for Environmental Prediction's (NCEP) Global Data Assimilation
173 System (GDAS) (GDAS; Kanamitsu,1989) with the HYSPLIT program (HYSPLIT; Stein et al.,
174 2015) using the Stochastic Time Inverted Lagrangian Transport Model (STILT) (Fasoli et al.,
175 2018) in concentration mode for 100 particle tracers starting near the top of the marine boundary
176 layer. We use the STILT model in our analysis to gauge the extent to which the center of mass
177 trajectory that we derive from the dispersion of the tracers is a viable description of the likely
178 parcel track. We assume that as the particles disperse, the center of mass trajectory becomes less

179 informative of the likely path of the air mass. We use standard deviational ellipses to determine
180 the extent of the particle dispersion within one standard deviation of the center of mass parcel
181 trajectory. We assume that the trajectory is not informative after the ellipse area reaches 40,000
182 km^2, equivalent approximately to a circle with a 224 km diameter. However, we continue to use
183 the trajectory for anecdotal information on airmass origin, recognizing the uncertainty. While the
184 cutoff size of the ellipse is arbitrary, it is approximately twice the area of a MODIS analysis
185 scene that we use for averaging. We reason that a trajectory uncertainty much larger than this
186 significantly influences our knowledge of the likely location of the airmass and the cloud
187 properties along the trajectory. We run HYSPLIT/STILT for each case study, storing data in 1-
188 hour intervals with the parcel's endpoint being the central latitude and longitude of the cloud
189 scene.
190 We use reanalysis data sets to describe the meteorology along trajectories from a
191 combination of MERRA-2 reanalysis data and the GDAS model output. MERRA-2 is based on
192 the MERRA system (GEOS-5.2.0) (Rienecker et al., 2011), with numerous updates described in
193 detail in Bosilovich et al., 2015. GDAS provides analyses four times a day and forecasts using
194 the Global Forecast System (GFS) (Abreu et al., 2012).
195 c. MODIS Data
196 The AQUA and TERRA satellites each pass over the high latitude SO region twice per
197 day but only once during daylight, providing potentially two views of the cloud field separated
198 by several hours (typically 4-6 hours). Terra usually passes over around 00 UTC or mid-local
199 morning, while Aqua passes closer to 06 UTC or in the early local afternoon. Moderate
200 Resolution Imaging Spectroradiometer (MODIS) level 2 cloud products (MOD06_L2) from
201 MODIS of the AQUA and TERRA satellites provide effective radius (r_e) and optical depth (τ)
202 during daytime from which LWP is derived (Platnick et al., 2003, 2015). We then use the
203 MODIS Level 2 retrievals of τ and r_e to calculate N_d with the method described by Grosvenor et
204 al. (2018), who assume an adiabatically shaped cloud profile among other assumptions. In Mace
205 et al. (2023), we evaluate and use the method outlined in Grosvenor et al. (2018), where we
206 examine the sources of error in the N_d computation from the MODIS retrievals concurring with
207 the analysis in Grosvenor et al. (2018) that a pixel level uncertainty of approximately 80% is
208 appropriate.

209 We use the same basic approach to sampling the MODIS data used in Mace et al. (2023),
210 where the MODIS data are filtered by solar and view zenith angles, cloud type, and coverage.
211 Every center-of-mass point along a trajectory is assigned a nearest MODIS scene in space and
212 time where a scene is a set of 1-km MODIS pixels in 1° latitude by 2° longitude regions. Only
213 when the MODIS scene is reliably composed of low-level clouds as described in Mace et al.
214 (2023) and is within 180 km and 4 hours of a trajectory point, do we use the scene in further
215 analysis. In a scene, we store the statistics of cloud properties (LWP, τ, r_e, and N_d). Over a
216 trajectory we tend to find clusters of 1 to 3 MODIS overpasses between 00 and 06 UTC each day
217 allowing for a coarse time series of spatially averaged cloud properties along the trajectory paths.
218 We also directly compare the cloud properties retrieved from MODIS with those derived from
219 the ship-based remote sensors. For this comparison, we typically focus on a 50 km diameter set
220 of pixels centered on the ship.
221

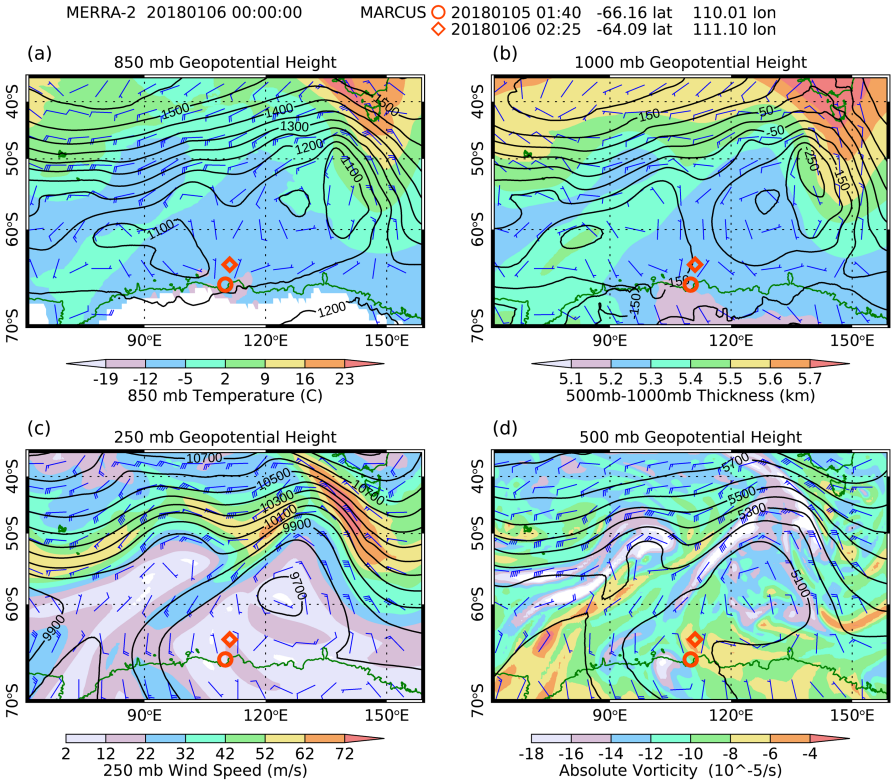

Figure 1. Large-scale meteorology from MERRA-2 during the January 5 and 6 case studies. Location of the ship during the January 5 Terra overpass is marked with a red circle. A red diamond marks the location of the ship on January 6. a) 850 hPa geopotential heights (contours, meters), and 850 hPa temperatures (color shading), b) 1000 hPa geopotential height (contours, m) and 500-1000 hPa thickness (km), c) 250 hPa geopotential height (contours, m) and wind speed, d) 500 hPa Geopotential height (contours, m) and absolute vorticity

222

223

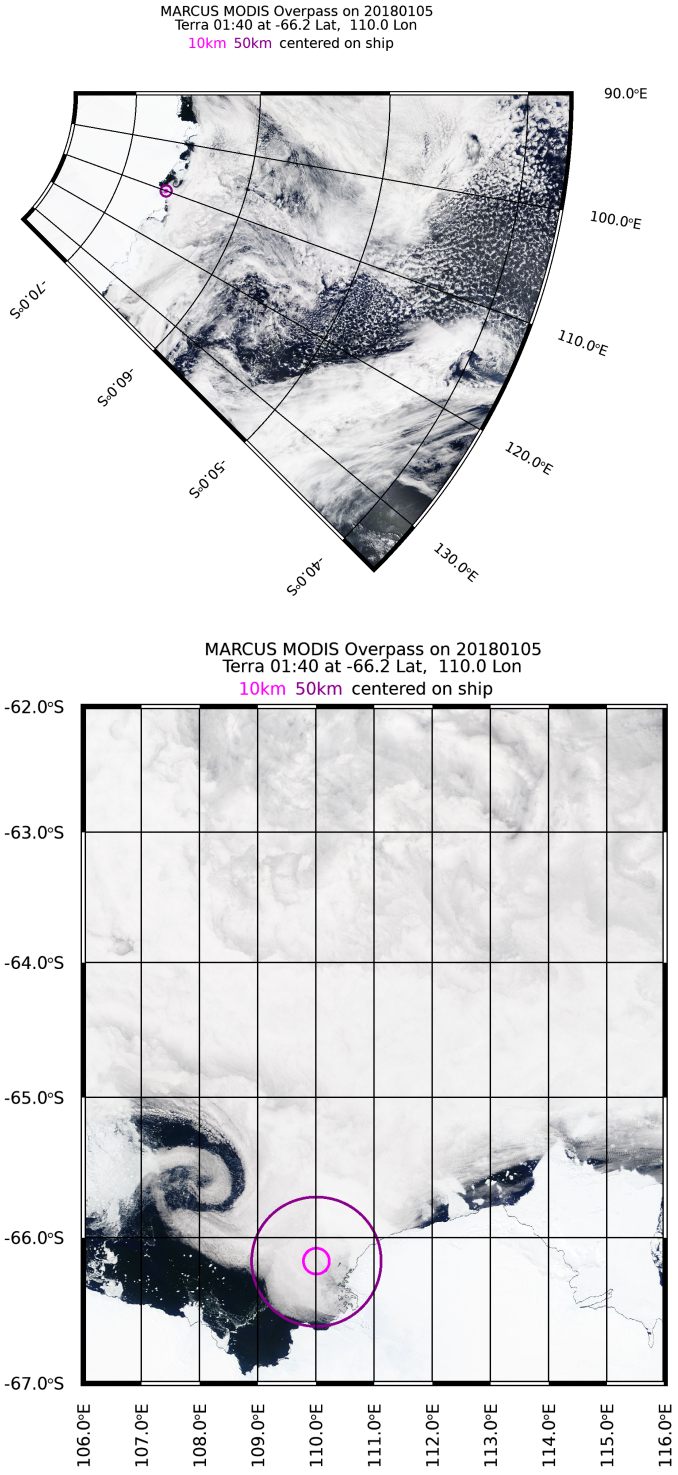

Figure 2. Terra MODIS imagery (3-color visible composite) collected at 0140 UTC January 6, 2018. Ship location shown by concentric 10 and 50 km circles.

We present three case studies - two from the Marcus Campaign and one from Capricorn II. In choosing these case studies, we sought examples that illustrate the statistical findings in Mace et al. (2021 and 2023) and presented in Section 4 of this paper where cloud properties derived from satellite measurements demonstrate a gradient in cloud properties with distance from the Antarctic coast. These case studies had high view-zenith MODIS overpasses of the ship that allows us to establish the validity of derived cloud properties by comparing the MODIS scene statistics with cloud properties derived from the surface-based data. The first two case studies we present are derived from a consecutive 30-hour period during Marcus. We present it as two case studies because the ship, while transiting northeast, sampled two distinctly different air masses that had very different histories and very different cloud and aerosol properties. Case Study 1 is the 12-hour period from 00 UTC until 16 UTC on 1/5 while Case Study 2 begins at ~20 UTC on 1/5 and extends until 05 UTC on 1/6. Case study 3 is from the Capricorn II campaign and extends over a two-day period on the fourth and fifth of February 2018.

3.1 January 5, 2018 - Marcus

The first case study is from data collected on 5 January 2018 (hereafter 1/5) when the Aurora Australis was heading away from Casey Station on a return trip to Hobart. The ship had recently spent nearly a week at Casey and collected atmospheric data as part of Marcus during the port period, as discussed in Mace et al. (2021) where we noted a persistent BL cloud deck with relatively high N_d in an offshore flow. The large-scale atmospheric state at 00 UTC on 1/6 features a jet stream oriented well north along 50°S, and a broad region of weak low pressure with little thermal contrast oriented in a broad trough along 60°S placing the Wilkes Land region of the East Antarctic Coast in a weak easterly flow.

The cloud field observed by MODIS on Terra at 0140 UTC in the region of the Aurora Australis on 1/5 (Fig. 2) shows an extensive BL cloud field with the ship located south-east of a mesoscale cyclonic feature that was also observed in the MODIS Aqua overpass at 07 UTC on this day that gives the appearance of a terrain-induced coastal low. A close examination of the image reveals many small-scale vortices in the near shore closed-cell stratocumulus likely associated with the easterly flow interacting with the complicated coastal geography. Offshore, the closed cellular pattern appears to become more cumuliform with an open cellular structure north of the trough axis along 60°S.

255 The local meteorology observed by instruments on the ship and 6-hourly soundings (not
256 shown) document an ~5 m/s northeasterly wind with surface temperatures near -2°C. The
257 potential temperature difference between the surface and the 850 hPa layer was 8°C. The
258 boundary layer was well mixed up to an inversion based near 1 km, and the clouds had a
259 temperature near -10°C. Photos and video recorded during this day (not shown) show calm seas
260 with only scattered sea ice and mostly open water under a persistent low overcast.

261

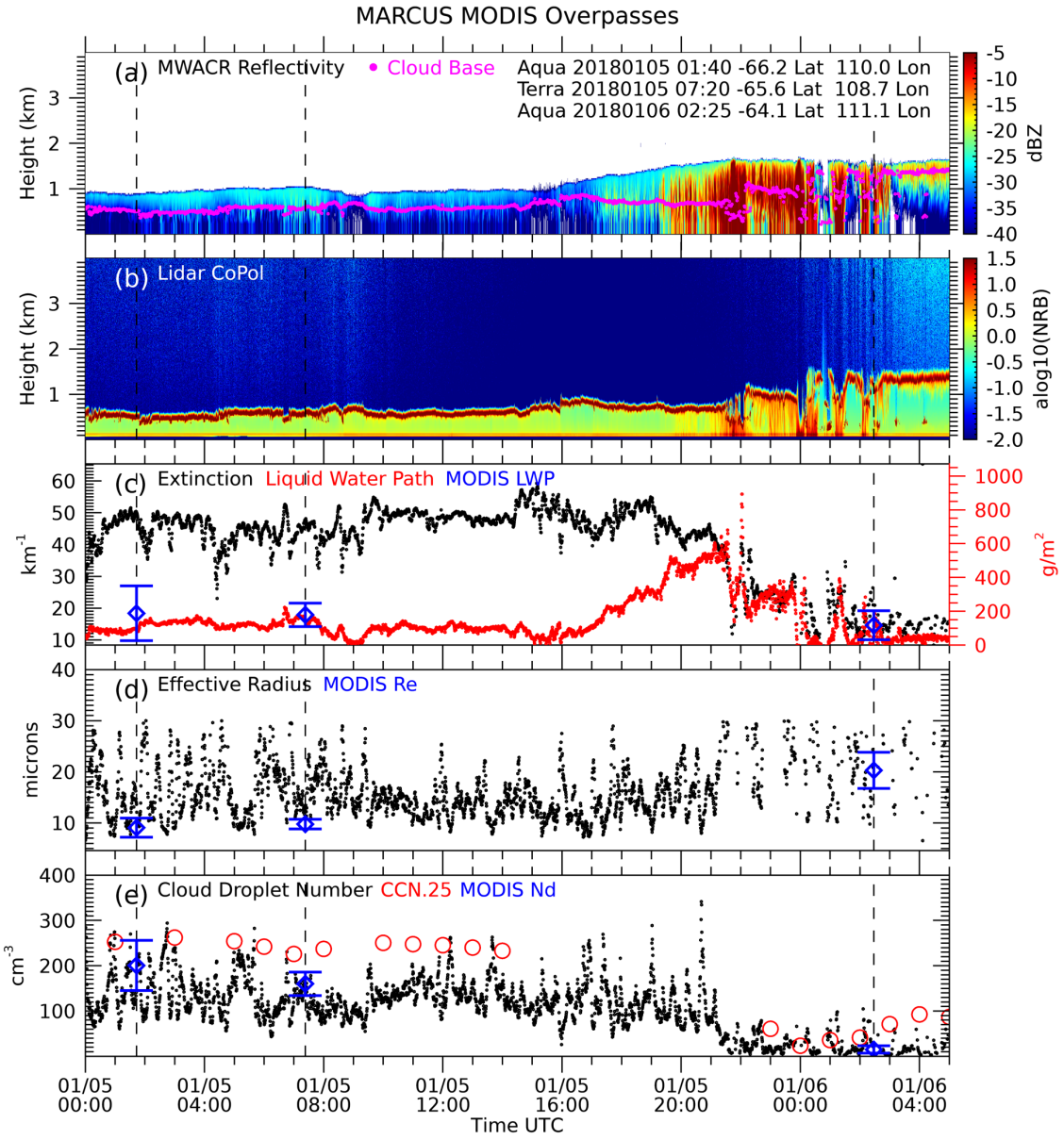

Figure 3. Marcus Surface measurements and derived cloud properties collected from aboard the Aurora Australis on January 5 and 6, 2018. a) w-band radar reflectivity with ceilometer cloud base overlaid (purple), b) lidar copolar attenuated backscatter, c) visible extinction derived from the lidar data using the method of Li et al. (2011), d) effective radius (black) and liquid water path (red), e) cloud droplet number concentration (black) and hourly averaged CCN at 0.25% supersaturation (red circles). MODIS overpass averages and standard deviations shown as blue circles with error bars to indicate standard deviation of 50 km domain centered on the ship.

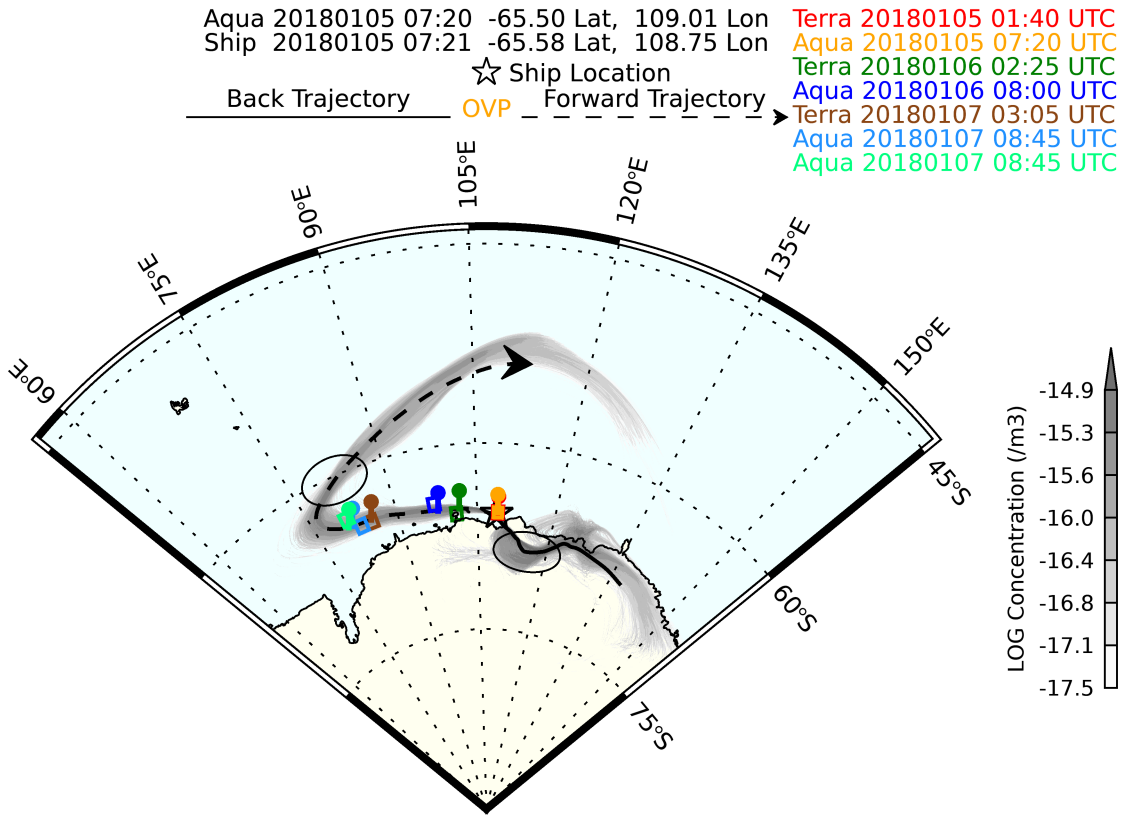

Figure 4. 5-day Hysplit backwards and forwards trajectories from the Marcus ship location (star). The solid and dashed curves show the center-of-mass trajectory from the tracer concentrations (gray). Drop pins denote MODIS overpasses over water with color code corresponding to inset information at the bottom of the figure. The ellipses denote the point in the trajectories where the concentration of tracers denote significant uncertainty in the center of mass trajectory (see text for explanation).

A time series of remote sensing and derived cloud properties in Fig. 3 show an optically thick cloud layer that fully attenuates the lidar. We note that a transition in observed and derived cloud properties begin near 16 UTC on 1/5. This transition period occurs as the ship transits northeastward and encounters an airmass with very different history as discussed below. From

266 00 to 16 UTC, the layer base is near 600 m, with tops near 1 km. The liquid water path (LWP)
267 derived from the microwave radiometer suggests an approximate 2-hour periodicity in enhanced
268 LWP that correlates with periods of episodic drizzle occurring during the high LWP part of the
269 day. The more extended period oscillations in LWP are also matched in the lidar-derived
270 extinction. On a much more rapid pace, we note oscillations in cloud droplet number Nd, r_e, and
271 lidar-derived extinction. These oscillations are approximately in phase with the drizzle events
272 that had a timescale of 10-15 minutes. Overall, extinction's high (low) values correlate with
273 local maxima (minima) in N_d. The r_e is anticorrelated with N_d, but these quantities are not
274 independent in the retrieval algorithm. We find that the MODIS retrievals are in reasonable
275 agreement with the surface retrievals regarding the mean values and the variability. The
276 depolarization ratio of the lidar is poorly known below values of 0.4 due to a substandard
277 window that was repaired on 13 January, so we infer liquid drizzle based on the Doppler velocity
278 and the low radar reflectivity.
279 CCN remains in the 250 cm^{-3} range throughout case 1 - well beyond the 75th percentile of
280 CCN at 0.2% supersaturation for this latitude belt compiled from Capricorn II and MARCUS
281 data reported in Humphries et al. (2021). N_d ranges up to the values of the CCN in between

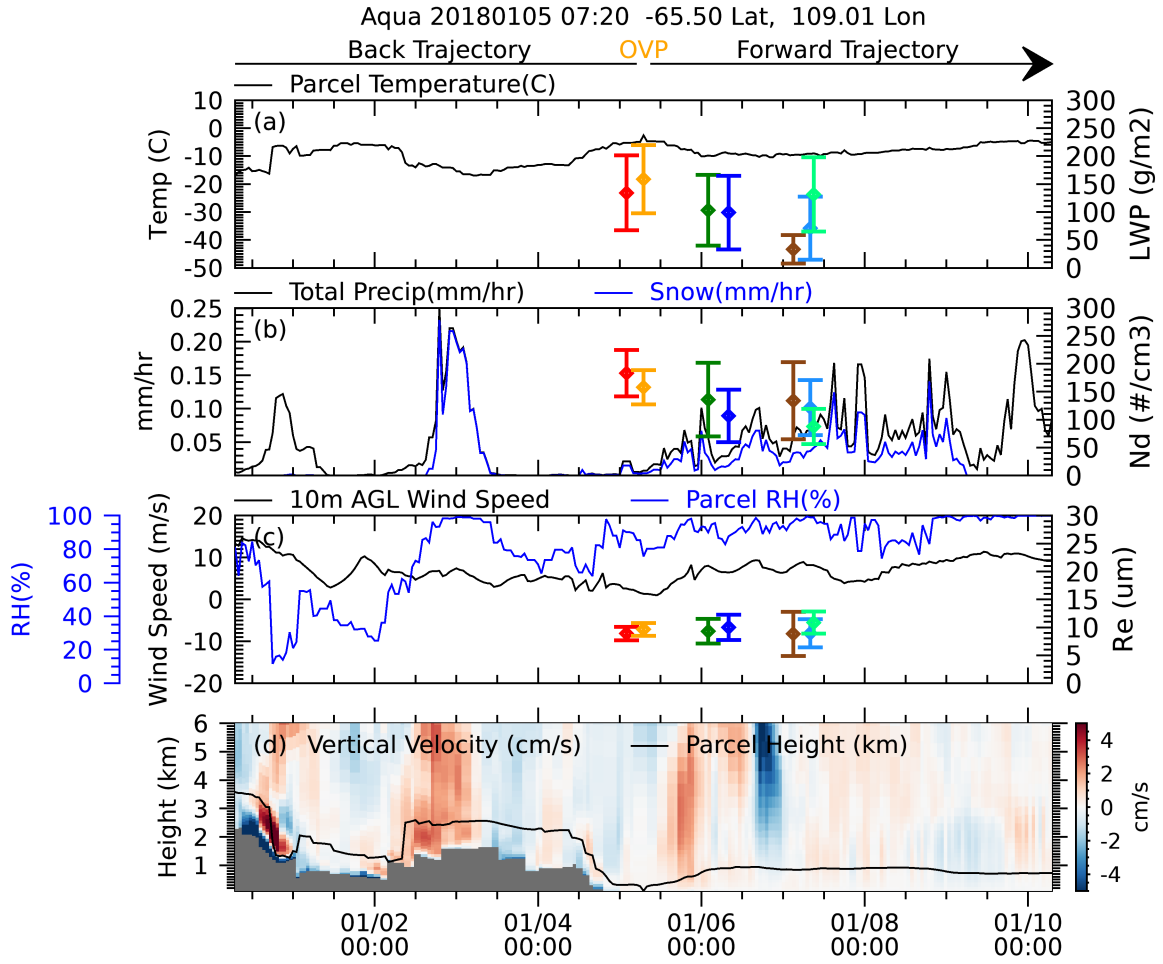

Figure 5. Meteorological quantities and MODIS cloud properties from along the backwards and forwards trajectories depicted in Fig. 4. OVP is the overpass time of the ship by MODIS Aqua on 07:20 UTC. A) Parcel temperature and MODIS LWP, b) Total and snow precipitation rates and MODIS Nd, c) Parcel relative humidity and 10 m wind speed and MODIS r_e, d) large-scale vertical motion and parcel height.

282 drizzle events to values as low as 80 cm^{-3} in regions near more intense drizzle where the
283 extinction is also a minimum.
284 Back trajectories (Figs. 4 and 5) show that the air mass had recently descended to near
285 the sea surface, as depicted in downward vertical motions along the parcel trajectory late on 1/4.

Before this, the trajectories suggest that the air mass transited the Law Ice Dome during the previous 48 hours near 2 km altitude and temperatures near -15°C. The MERRA-2 model suggests clear skies during the time over the Law Ice Dome, and this seems reasonable given the quiescent large-scale meteorology. While the back trajectories are quite uncertain during the back trajectory, there is an indication that before being over the Law Ice Dome, the air mass had been at a higher elevation over the ice sheet and then descended to near sea level, passing over the Totten Ice Shelf. Thus, it appears that the air mass had spent little time over the SO in the days before the case study period examined here.

The first cluster of MODIS overpasses of the trajectory are those that passed over the ship on 1/5. After that, two additional sets of overpasses occurred on 1/6 and 1/7. The cloud properties derived along the forward trajectories clustered in time show reasonable consistency in the scene-averaged r_e, N_d, and LWP. During the forward trajectory as the air mass continues roughly westward over the open ocean, the MODIS retrievals show little change in r_e although both LWP and N_d decreased over the ensuing three days. N_d drops from near 200 cm^{-3} during the overpasses of the ship on 1/5 to values near 100 cm^{-3} in the cluster of overpasses on 1/7. The MERRA-2 model suggests that light precipitation in the form of snow in the BL clouds increased after 1/5, consistent with decrease in N_d and LWP.

3.2 January 6, 2018 - Marcus

On the day following the 1/5 case study, January 6, 2018 (1/6), the Aurora Australis had progressed ~240 km to the northeast. They continued northeastward through open water with icebergs and wildely scattered sea ice notable on the video and still photography. The winds had increased and ranged between 10-15 m s^{-1} from the northeast during the early UTC hours of 1/6. The sea state remained unremarkable with no apparent whitecaps that would indicate active sea salt aerosol production locally. Surface temperatures were near and just below freezing, having warmed slightly from the previous day. The sounding at 06 UTC (not shown) shows that the boundary layer had deepened considerably yet remained well mixed with the base of the marine inversion near 1.6 km. The clouds observed by the ARM remote sensors (Fig. 3) show a marked contrast from the previous day with a transition in cloud properties that began at ~16 UTC and was complete by 00 UTC. A persistent layer of BL clouds continues with bases now near 1.4 km

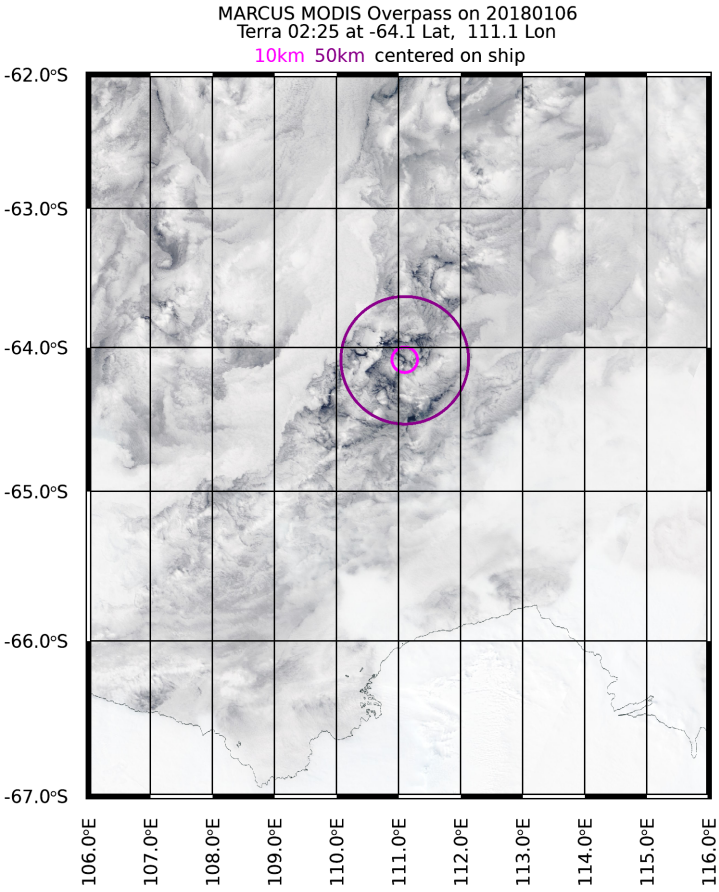

Figure 6. As in Figure 2b but for the Terra MODIS overpass at 02:25 UTC on 1/6.

and with layer top at the bottom of the marine inversion at temperatures near -15ºC. Higher radar reflectivities are noted in precipitation that, according to lidar depolarization above 0.4 during events before 03 UTC, seems to be snow. After 03 UTC, we cannot establish with certainty the phase of the lighter precipitation because of ambiguity in the lidar depolarization noted earlier. The cloud field is variable before 03 UTC, with breaks in the lidar data and lower cloud bases in heavier precipitation. Widely scattered clouds are observed below the bottom of the primary cloud layer.

The variability in the cloud field is consistent with satellite imagery and photography recorded at the ship (Figs. 6 and 7). The MODIS overpass at 0225 UTC places the ship in a region of mostly overcast cloud cover with the sea surface visible in various breaks in the cloud field in the vicinity of the ship. A photograph (Fig. 7) taken at 0226 UTC at the approximate

328 time of the MODIS overpass looks towards the northeast and shows thick boundary layer clouds
329 with breaks in the layer.

Figure 7. Photograph taken from the Aurora Australis at 02:26 UTC on 1/6 near the time of the MODIS overpass. Perspective is looking northeast.

330 The derived cloud microphysical properties had also changed considerably from 1/5. N_d
331 is overall much lower, ranging between 10 and 50 cm^{-3} with substantial variability in regions of
332 precipitation (Fig. 3). These values of N_d are in broad agreement with MODIS, which records a
333 mean of ~15 cm^{-3}. The effective radius is also larger than on 1/5 and is in the 20-30 um range
334 from the surface, while MODIS retrieves a value near 20. um. LWP is highly variable in and
335 around precipitation, reaching several hundred g m^{-2}. After 03 UTC, the cloud properties
336 become much more steady as the ship moves into the less variable cloud field to the northeast in
337 Fig. 6. However, light precipitation from the cloud continues. The derived cloud properties also
338 continue to show markedly low N_d and high r_e, with the LWP now in the 50 g m^{-2} range,
339 suggesting that the cloud properties feature low N_d and high r_e throughout this area and not just
340 in regions of active precipitation.
341 The 5-day back trajectories (Fig. 8) suggest that the air mass had exited continental
342 Antarctica near the beginning of the 5-day period on January 1 and likely came from the region
343 of the Amery Ice Shelf in what is known as Prydz Bay. The trajectories are substantially

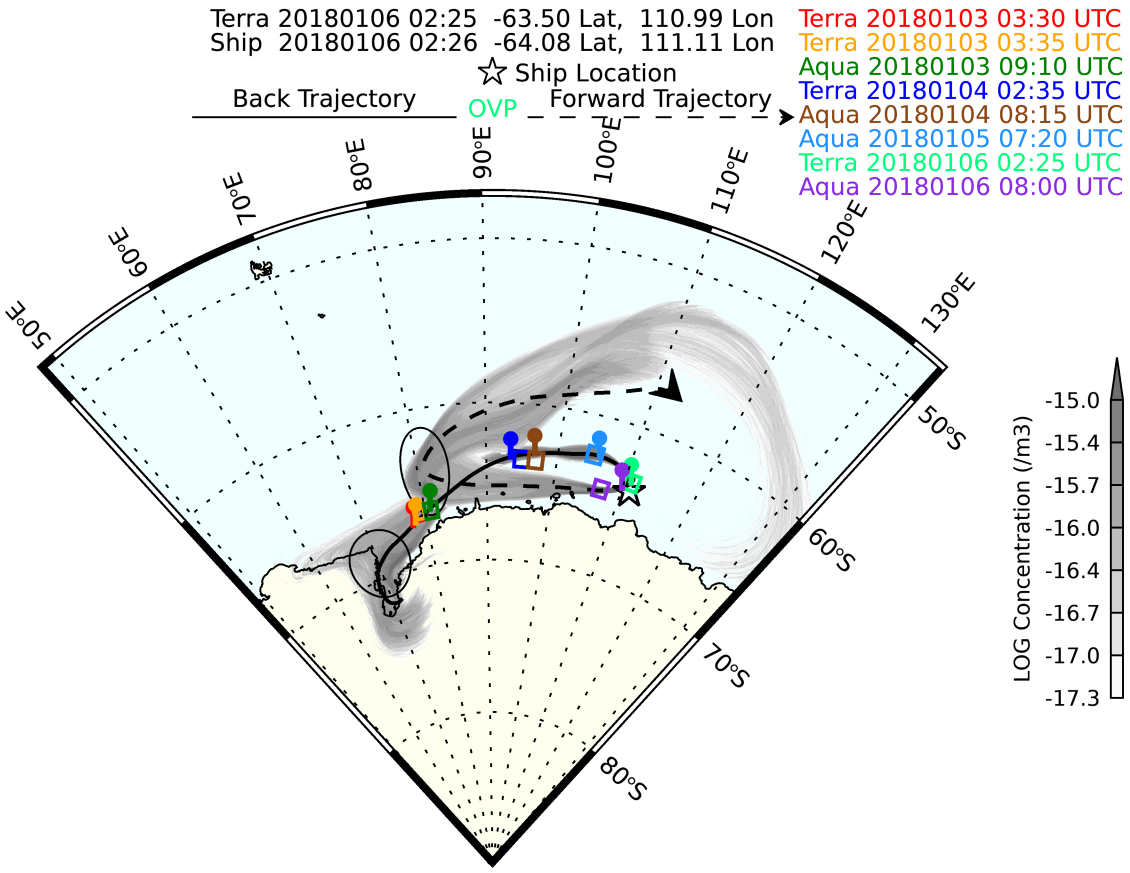

Figure 8. As in Figure 4 except for 1/6.

344 uncertain. However, the majority of the individual trajectories do show this path. Other parcels
345 follow the coastline near the Amery ice shelf. We can confidently say that the air had been over
346 open water for most of the past five days. There is a well-defined trend in MODIS cloud
347 properties along the trajectory. We pick up the first set of MODIS overpasses of open water
348 early on January 3 and have 4 clusters of overpasses on each succeeding day until 1/6. On 1/3
349 the Nd was in the 200 cm^{-3} range (Fig. 9) with r_e near 8 um - similar to the values found on 1/5 in
350 the air that had recently descended from the Law Ice Dome. The N_d decreased, and the r_e
351 increased in each successive set of overpasses until 1/6. The LWP, on the other hand, shows a
352 different trend. MODIS records a Maximum LWP near 200 g m^{-2} early on 1/4 while a

353 minimum in LWP occurs 24 hours later. While it borders on speculation, the precipitation
354 (mostly snow) predicted by MERRA-2 seems to lag the LWP by about ½ day.

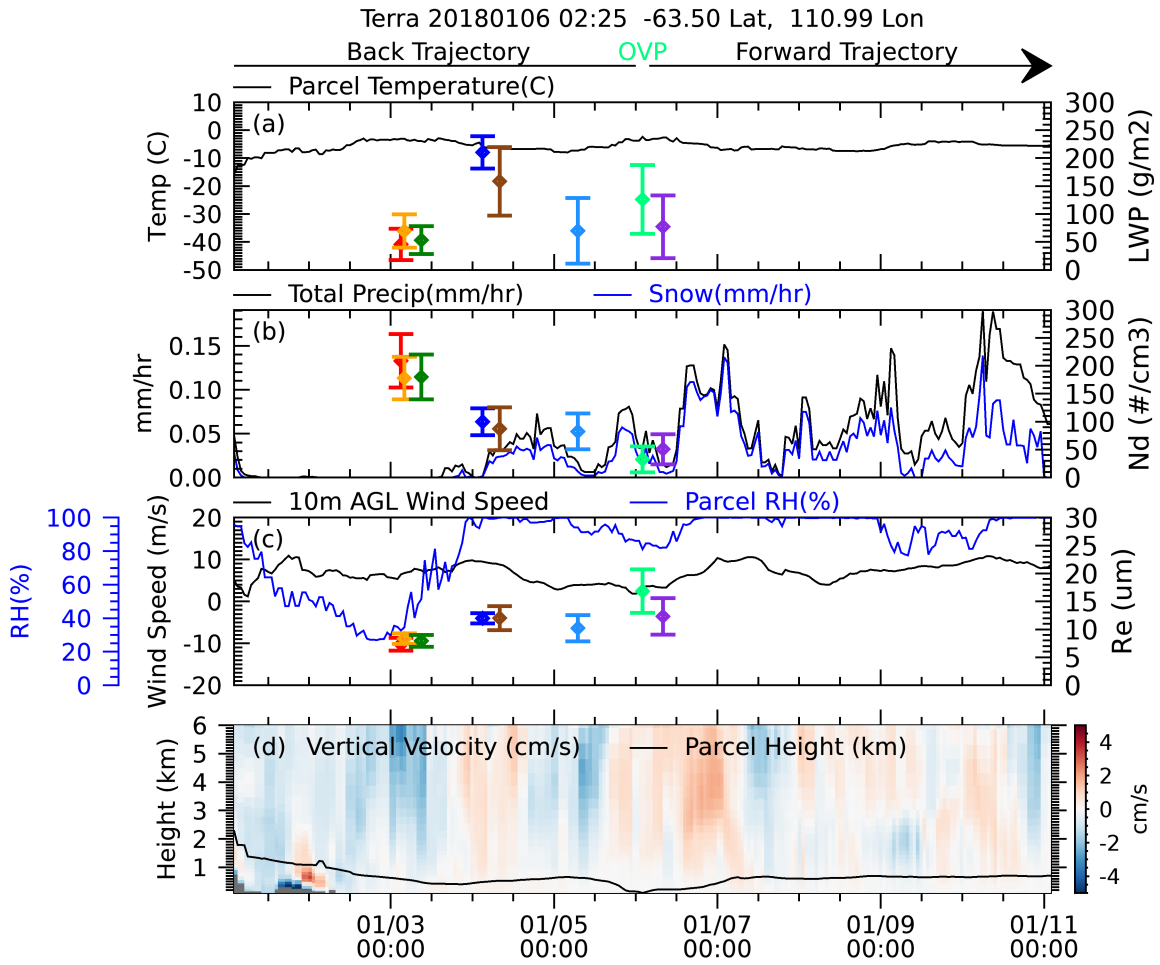

Figure 9. As in Figure 5 except for the 1/6 case study.

355 It is interesting to note in Fig. 3 that the ship time series of CCN (0.25% supersaturation)
356 during the 1/6 case study period. Recall that 24 hours prior, CCN was in the 250 cm^{-3} range and
357 close to the 90th percentile of CCN for this latitude band. While CCN is missing late on 1/5, the
358 cloud properties transition from the high N_d and small r_e on 1/5 to what is observed on 1/6. It
359 seems clear that the air mass sampled by the Aurora Australis shifted from one that had recently
360 emerged from continental Antarctica to an air mass that had experienced land multiple days prior
361 that now had much lower CCN and N_d.
362

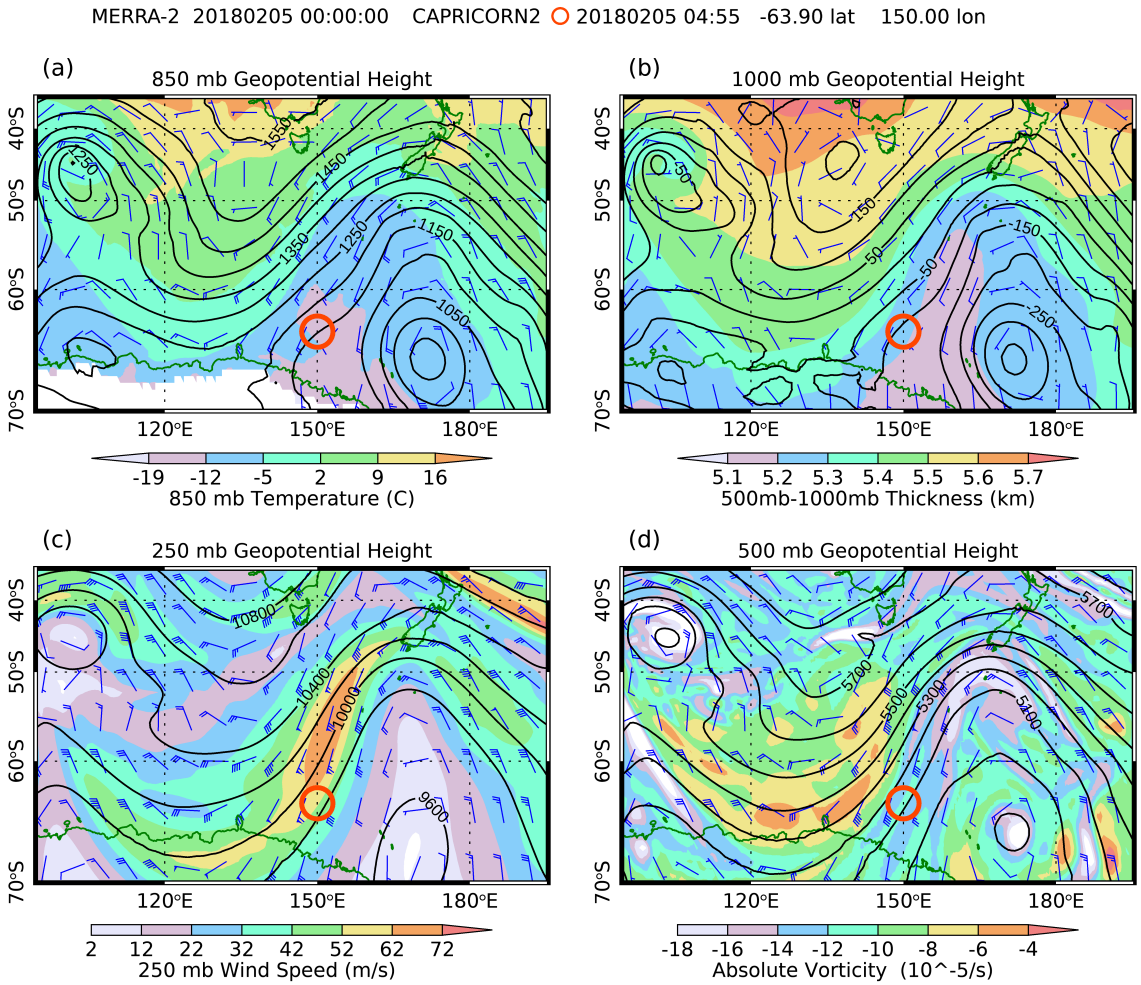

Figure 10. As in Fig. 1 except for the 2/4-2/5 case study. The red circle marks the location of the R/V Investigator on 2/5 at 00 UTC.

3.3 February 4 and 5, 2018 – Capricorn II

We take our final case study from data collected during the Capricorn II campaign on February 4 and 5, 2018 (2/4, 2/5) when the R/V Investigator was conducting oceanographic measurements within 100 km of 65°S, 150°E. The ship began a northward transit at 10 knots during midday on 2/5. The large-scale meteorology (Fig. 10) at 00 UTC on 2/5 shows a highly amplified upper-level pattern with a trough axis along 170°E and a ridge along about 130°E. A frontal system associated with the low pressure centered at 65°S, 170°E at 00 UTC 2/5 had

370 passed over the ship on 2/3 at around 15 UTC, turning the flow out of the south. By 00 UTC on
371 2/5, this southerly flow extended through the entire troposphere.

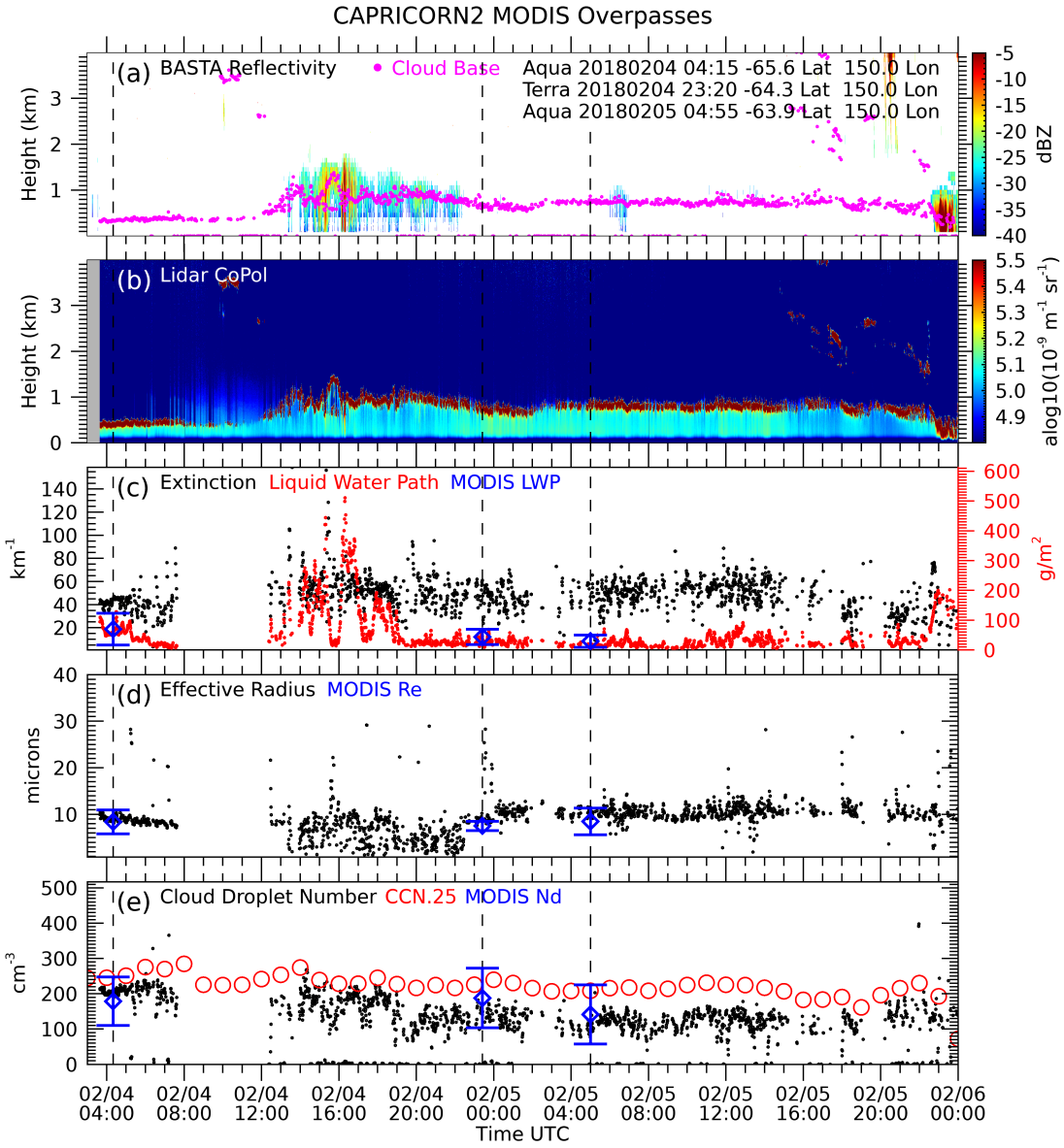

Figure 11. As in Figure 3 except for the 2/4-2/5 Capricorn II Case Study

372 Weather at the ship evolved somewhat during these two days. Surface temperatures
373 remained between -2° and -4°C, and surface winds were steady out of the south at 10-15 m s^{-1}.
374 Photography collected from the ship shows only modest wind waves, given the ship's proximity
375 to the sea ice edge with very scattered white caps, suggesting the possibility of some local sea

376 salt aerosol generation. A marine inversion was not evident in the 3-hourly soundings until 16
377 UTC on 2/4 when it was based near 1.5 km with a temperature of -15°C. The inversion
378 strengthened as the pattern progressed, and surface pressure rose through 2/5. By mid-day on
379 2/5, a strong marine inversion with a 10°C potential temperature difference between the surface
380 and 850 hPa was based near 1 km at a temperature of -10°C.

381 The BL clouds observed during this case study period (Fig. 11) were based near 500 m
382 and, except for a period between 15 UTC and 23 UTC on 2/4, the clouds were below the
383 detection threshold of the cloud radar on the R/V Investigator (~ -30 dBZe). The lidar shows a
384 mostly overcast cloud layer with some regions of broken clouds and optically thinner clouds
385 where the lidar transmits through the layer. Lidar depolarization ratios (not shown) in the sub-
386 cloud precipitation between 15 and 23 UTC appear to be primarily liquid except for two brief
387 episodes of snow that correlate with maxima in the radar reflectivity of more than -10 dBZe
388 between 15 and 16 UTC. MODIS imagery collected at 04 UTC on 2/4 and 05 UTC on 2/5 (Fig.
389 12) show the ship's position in relation to the cloud field. Cloud streets that formed as the
390 southerly flow encountered the sea surface and then evolved into closed cellular stratocumulus
391 are evident from the sea ice region to the south of the ship location. The cloud field remained
392 consistent during this southerly flow period.

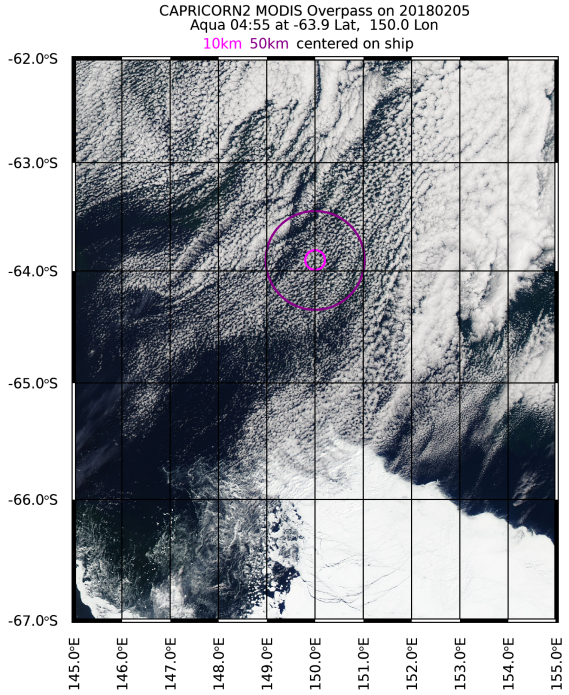

Figure 12. As in Fig. 2b except for a MODIS Aqua overpass of the 2/4-2/5 case study.

Derived cloud properties (Fig. 11) are also remarkably steady during the case study period. N_d decreases from near 200 cm^{-3} in the early part of the period to near 100 cm^{-3} after the light precipitation event at 19 UTC. CCN at 0.25% supersaturation remains steady throughout the case study between 200-300 cm^{-3}. This value of CCN, as the 1/5 case study presented earlier, is beyond the 90th percentile of CCN collected in this latitude belt. r_e follows N_d and remains at or below roughly 10 μm during most of the period. Except in the period with precipitation, the LWP remains in the 50-100 g m^{-2} range. Overall, the MODIS retrievals conducted from the overpasses agree reasonably with the surface-based cloud properties with high N_d and small r_e and LWP less than 50 g m^{-2} at the times of the overpasses. The MODIS N_d is well beyond the upper quartile of N_d recorded by MODIS during a 5-summer period examined in Mace et al. (2023).

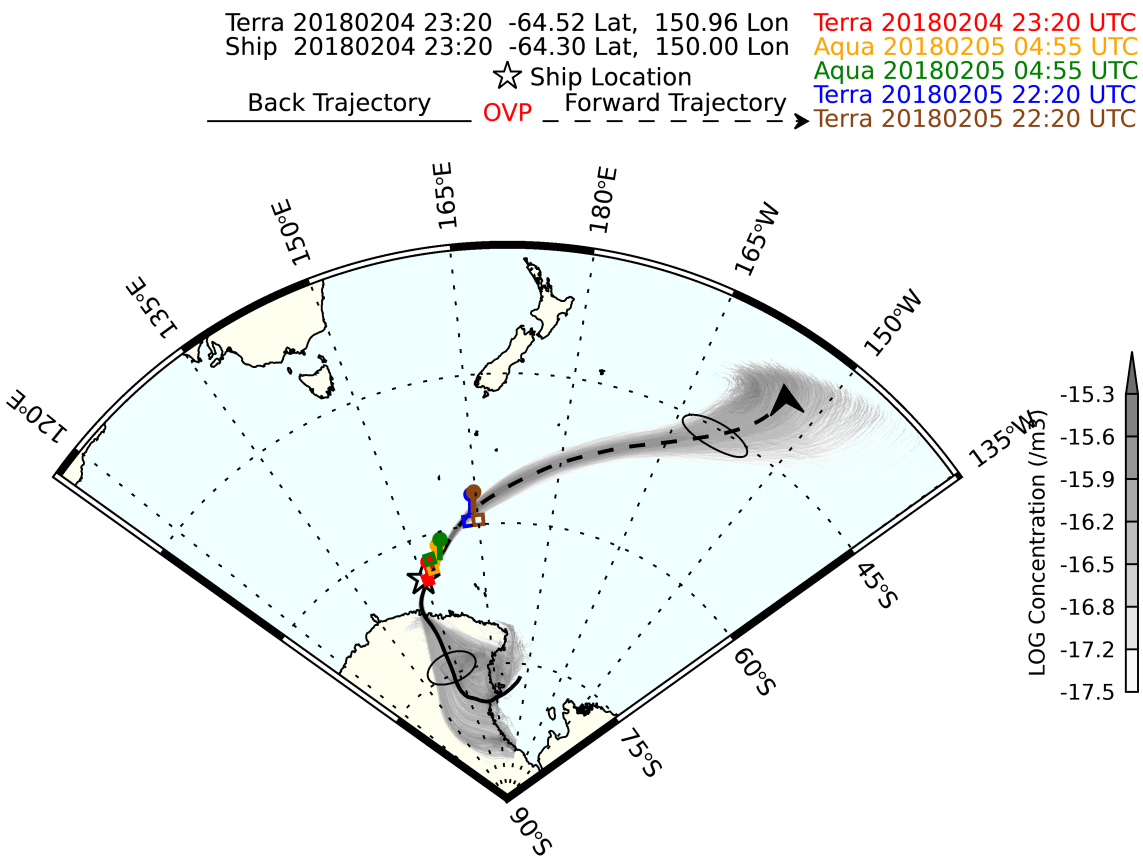

Figure 13. As in Fig. 5 except for 2/5 at 23 UTC.

As shown in Fig. 13, the air sampled during the case study period had spent the previous 48 hours transiting the high-altitude ice dome known as Dome C after it seemingly ascended from the Ross Sea. At least according to the back trajectories, the parcel was well into the free troposphere near 5 km altitude during this transit of Dome C, where predicted temperatures were near -40C. The air sampled at the ship had only been over the sea surface for a very short time after descending in a strong katabatic flow depicted in Fig. 14. After passing over the ship, the forward trajectories show that the air mass continued northeast. In addition to the overpasses near the ship, we find two additional sets of overpasses along the forward trajectory on 2/6 and 2/7. These show that the clouds evolved with increasing LWP and r_e and decreasing N_d to values of 70 cm^{-3} on 2/7.

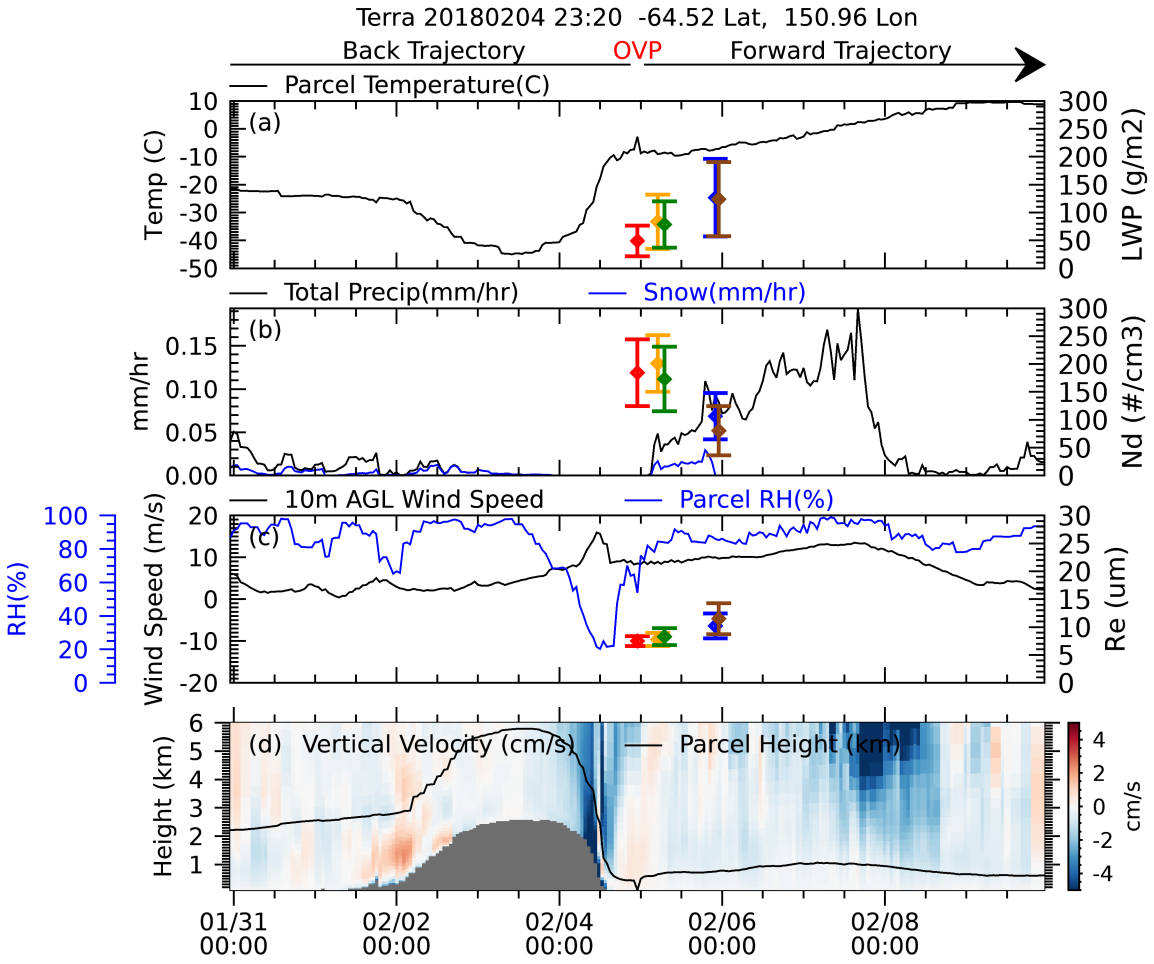

Figure 14. As in Fig. 5 except for 2/4 at 23 UTC.

The Capricorn II data included a Time-of-Flight Aerosol Chemical Speciation Monitor (TOF-ACSM) that allows for inference of aerosol composition. Humphries et al. (2021) present an analysis of the aerosol composition recorded as a function of latitude for recent Southern Ocean voyages. We show the compositional breakdown of the aerosol for the 2/4-2/5 case study in Fig. 15. We find that this aerosol mainly was (90%) sulfate and methanesulfonic acid (MSA). Very low values of other chemical species are indicated, including chloride – a proxy for sea salt. The sea salt and organic fraction of the aerosol composition in the 2/4-2/5 case study was less than half of that compared to the latitudinal average.

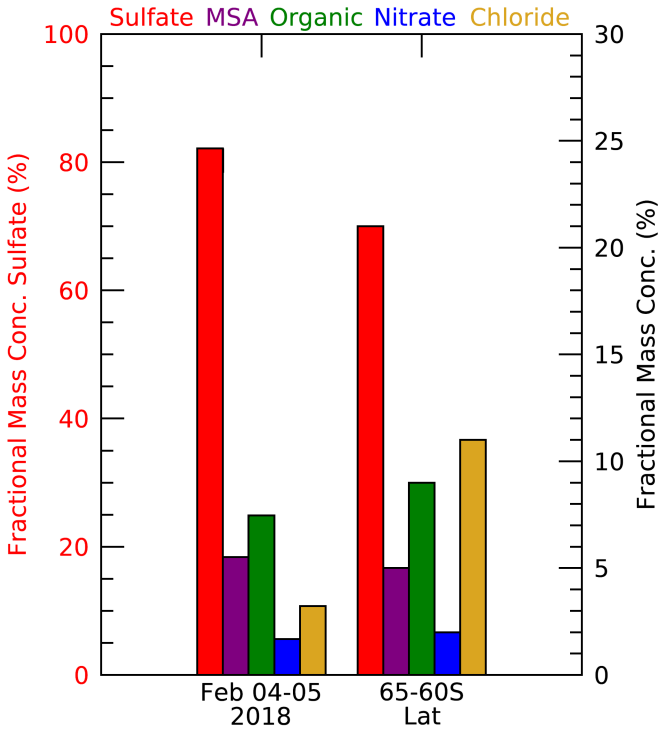

Figure 15. Aerosol compositional fractions from TOF-ACSM for the 2/4-5 case study compared to the latitudinal band average.

422

423 **4. MODIS statistics**

424 The three case studies we present seem to convey a picture consistent with the statistical
425 findings of Mace et al. (2021 and 2023) and the earlier results of Humphries et al. (2021 and
426 2016) and going back to Shaw (1988) that air masses that have spent significant time over the
427 Antarctic continental ice sheet emerge over the Southern Ocean with CCN concentrations in the
428 200-300 cm^{-3} range – significantly higher than the latitudinal average (Humphries et al., 2021).
429 To see how general this association is we examine MODIS data collected from Terra and Aqua

during Austral Summers (December through February) between 2014 and 2019 south of 60°S (the same data set used in Mace et al. 2023), except that here we examine the sensitivity of N_d in

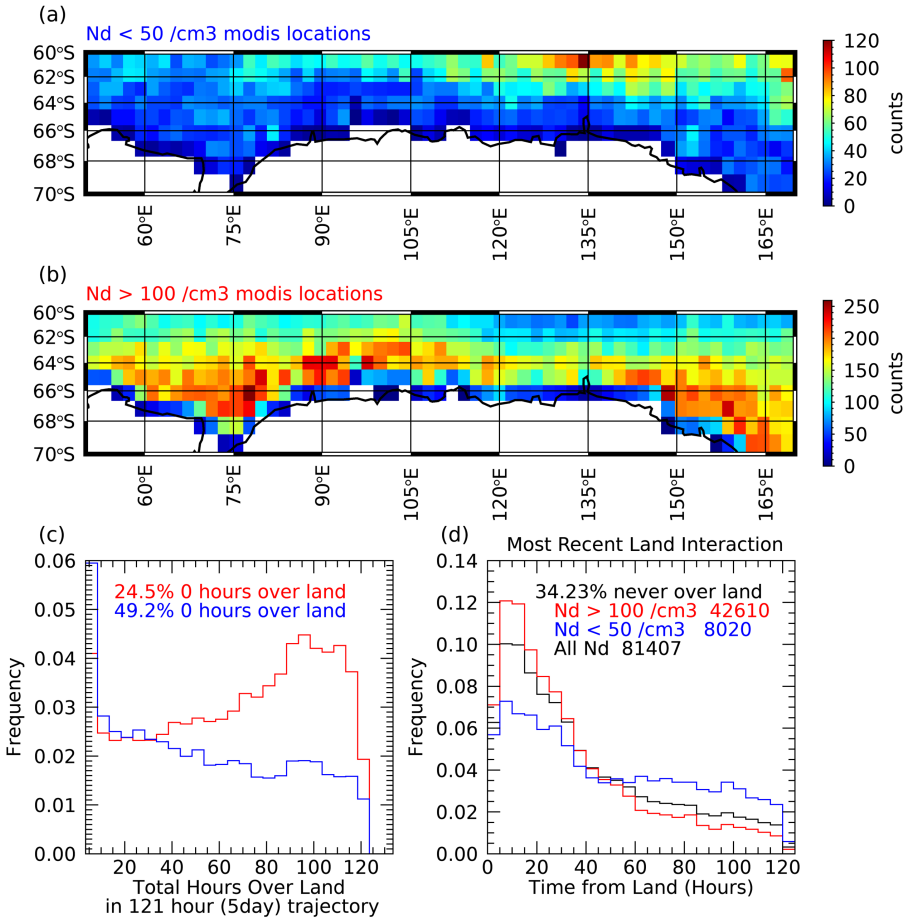

Figure 16. Occurrence of lower (a) and upper (b) Nd quartiles from MODIS data collected during the summers of 2014-2019. c) shows the frequency of occurrence of low (blue) and red (upper) Nd quartiles as a function of total hours spent over continental Antarctica in the 5-day back trajectory. d) shows the frequency of occurrence of the upper (red) and lower (blue) quartiles for over water scenes as a function of time since the back trajectory had encountered the Antarctic land mass.

a MODIS scene to the time since a back trajectory from that scene had encountered the Antarctic Continent. This analysis includes a total of 123784 trajectories. To demonstrate these relationships more clearly, we focus on the upper (100 cm^{-3}) and lower (50 cm^{-3}) N_d quartiles for all MODIS data in the Southern Ocean, as established in Mace et al. (2023).

The occurrence of the upper and lower N_d quartiles is strongly related to latitude (Fig. 16), with the high N_d quartiles tending to be adjacent to coastal Antarctica. Not surprisingly then, we also find that being in one or the other of the N_d quartiles is a strong predictor of the time since a back trajectory had encountered land (Fig. 16d). On the other hand, and perhaps less obviously, the amount of time spent over continental Antarctica seems to be predictive of membership in either the high or low N_d quartile. Nearly half of the low N_d quartile had not encountered land in the 5-day back trajectory, while only 25% of the high N_d quartile had been entirely over open water. Of the back trajectories that had passed over the continent, membership in either quartile depends oppositely on the amount of time spent over land. High N_d seems much more likely as time over the continent increases – rising sharply after 72 hours. On the other hand, low N_d is decreasingly likely as time over the continent increases.

5. Conclusions

While changes to model simulations of cloud feedbacks in the Southern Ocean are primarily responsible for the increased climate sensitivity of CMIP 6 (Zelinka et al., 2020), past work has documented that the cloud properties simulated in models are not consistent with observations of cloud properties Southern Ocean low-level clouds. Because cloud properties are strongly linked to precipitation this lack of consistency between models and observations calls into question the validity of the increased climate sensitivity. Fundamental to this is that the models seem to lack a mechanism to create the observed CCN concentrations (McCoy et al., 2021) over the summertime Southern Ocean. While the primary mechanism behind the high concentrations of CCN is likely related to aerosol nucleation and subsequent growth associated with sulfate precursor gasses emitted by the highly productive ocean biology in the high latitudes, the exact mechanism for the CCN production has not been established and are not simulated in global models of CCN production (Dunne et al., 2016; Lee et al., 2013). In this paper, we build on past work to show that air masses emerging into the MBL over the Southern Ocean after having spent time transiting the continental ice sheets of Antarctica during summer appear predisposed to have anomalously high CCN concentrations and produce clouds that have similarly anomalously high N_d.

Statistics derived from MODIS data demonstrate the relationship between time over Antarctica and high N_d clouds. These statistics are consistent with three case studies collected during ship-based observing campaigns in the Summer of 2018. A case on January 5, 2018, from the Marcus campaign and the 2/4-2/5 case from Capricorn II were of air masses that had recently emerged over the Southern Ocean after spending multiple days over continental Antarctica and had N_d from both MODIS and surface-based retrievals well within the upper quartile of what we find from multi-year MODIS analysis (> 100 cm^{-3}). CCN observed at the surface in the case studies was also anomalously high relative to the mean in the southern high latitudes. In both cases, the N_d along the trajectories decrease with time as the air masses transit over the open ocean and are diagnosed to no longer have N_d that would place it in the upper N_d quartile. On the other hand, the air mass sampled in the 1/6 case from Marcus had not been in contact with land for at least five days, and Nd from both surface and MODIS put it well within the lower N_d quartile. However, MODIS data from along the back trajectories suggest that N_d had decreased from values that placed it within the upper N_d quartile near the start of the 5-day back trajectory after the airmass likely emerged onto the Southern Ocean from the continental landmass.

The relationship between summertime transits of air masses over the continent and the production of high CCN air masses has been described in the literature (Shaw, 1988; Humphries et al., 2016). The highly productive waters of the Antarctic continental shelf produce copious precursor gasses beginning as DMS from phytoplankton along with oxidants such as BrO and IO. These maritime air masses would also contain preexisting primary and secondary aerosols such as sea salt and organics. Under synoptic scale conditions conducive to forced ascent, these air masses ascend the ice domes, where cloud and precipitation processes scavenge most of the ambient aerosol from these air masses. The air masses with high concentrations of aerosol precursor gasses now devoid of ambient aerosol then spend multiple days in the free troposphere at cold temperatures and extremely high actinic flux, enabling new particle formation and growth (Raes, 1995). Growth from the nucleation mode to CCN sizes would take several days, so long trajectories over the ice are favored. The air masses, now with high CCN, descend off the ice sheets in katabatic flows to the Southern Ocean marine boundary layer, forming the high N_d clouds found in observations.

While aspects of this storyline are speculative (the new particle formation process has not been observed in the free troposphere over the ice sheets, for instance), the critical elements of the story are reasonably well documented in past literature or cases and statistics presented in this paper. Additional observations are needed to establish this mechanism's validity more rigorously. It is fortuitous that several upcoming campaigns into the Southern Ocean are planned during this decade (Mallet et al., 2023). What is not planned but needed are airborne campaigns into the high latitudes to document the chemical pathways favored in taking aerosol precursor gasses to new particles that then grow into CCN and eventually seed the high albedo clouds observed by satellite and ground-based sensors.

Acknowledgements

This research was supported primarily by the U. S. Department of Energy's Atmospheric Systems Research, an Office of Science Biological and Environmental Research program, under Grant DE-SC00222001. This work was also supported by NASA Grant 80NSSC21k1969 and National Science Foundation (NSF) Grant 2246488. Data were obtained from the Atmospheric Radiation Measurement (ARM) User Facility, a U.S. Department of Energy (DOE) Office of Science User Facility managed by the Biological and Environmental Research Program. Technical, logistical, and ship support for MARCUS were provided by the Australian Antarctic Division through Australia Antarctic Science projects 4292 and 4387 and we thank Steven Whiteside, Lloyd Symonds, Rick van den Enden, Peter de Vries, Chris Young and Chris Richards for assistance. The authors would like to thank the staff of the Australian Marine National Facility for providing the infrastructure and logistical and financial support for the voyages of the RV Investigator. Funding for these voyages was provided by the Australian Government and the U.S. Department of Energy.

Open Research

All data used in this study are available in public archives. MARCUS data are available from the DOE ARM archive at https://adc.arm.gov/armlogin/login.jsp, SOCRATES data are available at https://data.eol.ucar.edu/project/SOCRATES, and CAPRICORN I and II data are available at

https://doi.org/10.25919/5f688fcc97166. MODIS cloud products can be found for Terra and Aqua at https://doi.org/10.5067/TERRA/MODIS/L3M/CHL/2018 and https://doi.org/10.5067/MODIS/MYD06_L2.006. GDAS data are obtained from ftp://ftp.arl.noaa.gov/pub/archives/gdas (National Centers for Environmental Prediction, 2022). Computer code for this study including analysis code and graphic generation code is available at https://doi.org/10.7278/S50d-bpx8-gmtt.

References

Albrecht, B. A. (1989). Aerosols, cloud microphysics, and fractional cloudiness. *Science*, *245*(4923), 1227–1230. https://doi.org/10.1126/science.245.4923.1227

Armour, K. C., Marshall, J., Scott, J. R., Donohoe, A., & Newsom, E. R. (2016). Southern Ocean warming delayed by Circumpolar Upwelling and Equatorward Transport. *Nature Geoscience*, *9*(7), 549–554. https://doi.org/10.1038/ngeo2731

Bodas-Salcedo, A., Hill, P. G., Furtado, K., Williams, K. D., Field, P. R., Manners, J. C., Hyder, P., & Kato, S. (2016). Large contribution of supercooled liquid clouds to the solar radiation budget of the Southern Ocean. *Journal of Climate*, *29*(11), 4213–4228. https://doi.org/10.1175/jcli-d-15-0564.1

Bosilovich MG, Akella S, Coy L, Cullather R, Draper C, Gelaro R, Kovach R, Liu Q, Molod A, Norris P, Wargan K, Chao W, Reichle R, Takacs L, Vikhliaev Y, Bloom S, Collow A, Firth S, Labow G, Partyka G, Pawson S, Reale O, Schubert SD, Suarez M (2015) MERRA-2: initial evaluation of the climate, technical report series on global modeling and data assimilation, vol 43, NASA/TM–2015-104606/Vol. 43, pp 136. http://gmao.gsfc.nasa.gov/reanalysis/MERRA-2/docs/

Clarke, A. D. (1993). Atmospheric nuclei in the Pacific midtroposphere: Their nature, concentration, and evolution. *Journal of Geophysical Research*, 98(D11), 20633–20647. https://doi.org/10.1029/93jd00797

Comstock, K. K., Wood, R., Yuter, S. E., & Bretherton, C. S. (2004). Reflectivity and rain rate in and below drizzling stratocumulus. *Quarterly Journal of the Royal Meteorological Society*, *130*(603), 2891–2918. https://doi.org/10.1256/qj.03.187

Dunne, E. M., Gordon, H., Kürten, A., Almeida, J., Duplissy, J., Williamson, C., Ortega, I. K., Pringle, K. J., Adamov, A., Baltensperger, U., Barmet, P., Benduhn, F., Bianchi, F.,

Breitenlechner, M., Clarke, A., Curtius, J., Dommen, J., Donahue, N. M., Ehrhart, S., … Carslaw, K. S. (2016). Global Atmospheric Particle Formation from CERN cloud measurements. *Science*, *354*(6316), 1119–1124. https://doi.org/10.1126/science.aaf2649

Eyring, V., Bony, S., Meehl, G. A., Senior, C. A., Stevens, B., Stouffer, R. J., & Taylor, K. E. (2016). Overview of the coupled model intercomparison project phase 6 (CMIP6) experimental design and organization. *Geoscientific Model Development*, *9*(5), 1937–1958. https://doi.org/10.5194/gmd-9-1937-2016

Fasoli, B., Lin, J. C., Bowling, D. R., Mitchell, L., & Mendoza, D. (2018). Simulating atmospheric tracer concentrations for spatially distributed receptors: Updates to the stochastic time-inverted lagrangian transport model's R interface (stilt-R version 2). *Geoscientific Model Development*, *11*(7), 2813–2824. https://doi.org/10.5194/gmd-11-2813-2018

Gettelman, A., Hannay, C., Bacmeister, J. T., Neale, R. B., Pendergrass, A. G., Danabasoglu, G., Lamarque, J. -F., Fasullo, J. T., Bailey, D. A., Lawrence, D. M., & Mills, M. J. (2019). High climate sensitivity in the Community Earth System Model Version 2 (CESM2). *Geophysical Research Letters*, *46*(14), 8329–8337. https://doi.org/10.1029/2019gl083978

Huang, Y., Siems, S. T., & Manton, M. J. (2021). Wintertime in situ cloud microphysical properties of mixed-phase clouds over the Southern Ocean. *Journal of Geophysical Research: Atmospheres*, *126*(11). https://doi.org/10.1029/2021jd034832

Huang, Y., Siems, S. T., Manton, M. J., Rosenfeld, D., Marchand, R., McFarquhar, G. M., & Protat, A. (2016). What is the role of sea surface temperature in modulating cloud and precipitation properties over the Southern Ocean? *Journal of Climate*, *29*(20), 7453–7476. https://doi.org/10.1175/jcli-d-15-0768.1

Humphries, R. S., Klekociuk, A. R., Schofield, R., Keywood, M., Ward, J., & Wilson, S. R. (2016). Unexpectedly high ultrafine aerosol concentrations above East Antarctic Sea Ice. *Atmospheric Chemistry and Physics*, *16*(4), 2185–2206. https://doi.org/10.5194/acp-16-2185-2016

Humphries, Ruhi S., Keywood, M. D., Gribben, S., McRobert, I. M., Ward, J. P., Selleck, P., Taylor, S., Harnwell, J., Flynn, C., Kulkarni, G. R., Mace, G. G., Protat, A., Alexander, S. P., & McFarquhar, G. (2021). Southern Ocean latitudinal gradients of cloud

condensation nuclei. *Atmospheric Chemistry and Physics*, *21*(16), 12757–12782. https://doi.org/10.5194/acp-21-12757-2021

Kang, L., Marchand, R. T., Wood, R., & McCoy, I. L. (2022). Coalescence scavenging drives droplet number concentration in Southern Ocean low clouds. *Geophysical Research Letters*, *49*(7). https://doi.org/10.1029/2022gl097819

Krüger, O., & Graßl, H. (2011). Southern Ocean phytoplankton increases cloud albedo and reduces precipitation. *Geophysical Research Letters*, *38*(8). https://doi.org/10.1029/2011gl047116

Lana, A., Simó, R., Vallina, S. M., & Dachs, J. (2012). Potential for a biogenic influence on cloud microphysics over the ocean: A correlation study with satellite-derived data. *Atmospheric Chemistry and Physics*, *12*(17), 7977–7993. https://doi.org/10.5194/acp-12-7977-2012

Lee, L. A., Pringle, K. J., Reddington, C. L., Mann, G. W., Stier, P., Spracklen, D. V., Pierce, J. R., & Carslaw, K. S. (2013). The magnitude and causes of uncertainty in global model simulations of cloud condensation nuclei. *Atmospheric Chemistry and Physics*, *13*(17), 8879–8914. https://doi.org/10.5194/acp-13-8879-2013

Mace, G. G., & Avey, S. (2017). Seasonal variability of warm boundary layer cloud and precipitation properties in the Southern Ocean as diagnosed from a-train data. *Journal of Geophysical Research: Atmospheres*, *122*(2), 1015–1032. https://doi.org/10.1002/2016jd025348

Mace, G. G., & Zhang, Q. (2014). The CloudSat radar-lidar geometrical profile product (rl-geoprof): Updates, improvements, and selected results. *Journal of Geophysical Research: Atmospheres*, *119*(15), 9441–9462. https://doi.org/10.1002/2013jd021374

Mace, G. G., Benson, S., Humphries, R., Gombert, P. M., & Sterner, E. (2023). Natural marine cloud brightening in the Southern Ocean. *Atmospheric Chemistry and Physics*, *23*(2), 1677–1685. https://doi.org/10.5194/acp-23-1677-2023

Mace, G. G., Protat, A., & Benson, S. (2021). Mixed-phase clouds over the Southern Ocean as observed from satellite and surface based Lidar and Radar. *Journal of Geophysical Research: Atmospheres*, *126*(16). https://doi.org/10.1029/2021jd034569

Mace, G. G., Protat, A., Humphries, R. S., Alexander, S. P., McRobert, I. M., Ward, J., Selleck, P., Keywood, M., & McFarquhar, G. M. (2021). Southern ocean cloud properties derived

614 from Capricorn and Marcus Data. *Journal of Geophysical Research: Atmospheres*,
615 *126*(4). https://doi.org/10.1029/2020jd033368
616 Mace, G. G., Zhang, Q., Vaughan, M., Marchand, R., Stephens, G., Trepte, C., & Winker, D.
617 (2009). A description of hydrometeor layer occurrence statistics derived from the first
618 year of merged Cloudsat and Calipso Data. *Journal of Geophysical Research:*
619 *Atmospheres*, *114*(D8). https://doi.org/10.1029/2007jd009755
620 Mallet, M. D., Humphries, R. S., Fiddes, S. L., Alexander, S. P., Altieri, K., Angot, H.,
621 Anilkumar, N., Bartels-Rausch, T., Creamean, J., Dall'Osto, M., Dommergue, A., Frey,
622 M., Henning, S., Lannuzel, D., Lapere, R., Mace, G. G., Mahajan, A. S., McFarquhar, G.
623 M., Meiners, K. M., … Woodhouse, M. T. (2023). Untangling the influence of Antarctic
624 and Southern Ocean Life on clouds. *Elementa: Science of the Anthropocene*, *11*(1).
625 https://doi.org/10.1525/elementa.2022.00130
626 McCoy, D. T., Burrows, S. M., Wood, R., Grosvenor, D. P., Elliott, S. M., Ma, P.-L., Rasch, P.
627 J., & Hartmann, D. L. (2015). Natural aerosols explain seasonal and spatial patterns of
628 Southern Ocean Cloud albedo. *Science Advances*, *1*(6).
629 https://doi.org/10.1126/sciadv.1500157
630 McCoy, I. L., Bretherton, C. S., Wood, R., Twohy, C. H., Gettelman, A., Bardeen, C. G., &
631 Toohey, D. W. (2021). Influences of recent particle formation on Southern Ocean aerosol
632 variability and low cloud properties. *Journal of Geophysical Research: Atmospheres*,
633 *126*(8). https://doi.org/10.1029/2020jd033529
634 McFarquhar, G. M., R. Marchand, C. Bretherton, S. Alexander, A. Protat, S. Siems, R. Wood
635 and P. DeMott, 2019: Measurements of Aerosols, Radiation, and Clouds over the
636 Southern Ocean (MARCUS) Field Campaign Report. DOE/SC-ARM-19-008. Available
637 at https://www.arm.gov/publications/programdocs/doe-sc-arm-19-008.pdf.
638 McFarquhar, G. M., Bretherton, C. S., Marchand, R., Protat, A., DeMott, P. J., Alexander, S. P.,
639 Roberts, G. C., Twohy, C. H., Toohey, D., Siems, S., Huang, Y., Wood, R., Rauber, R.
640 M., Lasher-Trapp, S., Jensen, J., Stith, J. L., Mace, J., Um, J., Järvinen, E., … McDonald,
641 A. (2021). Observations of clouds, aerosols, precipitation, and surface radiation over the
642 Southern Ocean: An overview of Capricorn, Marcus, MICRE, and socrates. *Bulletin of*
643 *the American Meteorological Society*, *102*(4). https://doi.org/10.1175/bams-d-20-0132.1

644 Morrison, A. K., Griffies, S. M., Winton, M., Anderson, W. G., & Sarmiento, J. L. (2016).
645 Mechanisms of southern ocean heat uptake and transport in a global Eddying Climate
646 Model. *Journal of Climate*, *29*(6), 2059–2075. https://doi.org/10.1175/jcli-d-15-0579.1
647 Platnick, S., King, M. D., Ackerman, S. A., Menzel, W. P., Baum, B. A., Riedi, J. C., & Frey, R.
648 A. (2003). The Modis Cloud Products: Algorithms and examples from Terra. *IEEE*
649 *Transactions on Geoscience and Remote Sensing*, *41*(2), 459–473.
650 https://doi.org/10.1109/tgrs.2002.808301
651 Platnick, S., Ackerman, S. A., King, M. D., Meyer, K., Menzel, W. P., Holz, R. E., Baum, B. A.,
652 and Yang, P.: MODIS Atmosphere L2 Cloud Product (06_L2), NASA MODIS Adaptive
653 Processing System, Goddard Space Flight Center, USA [data
654 set], https://doi.org/10.5067/MODIS/MYD06_L2.006, 2015.
655 Raes, F.: Entrainment of free tropospheric aerosols as a regulating mechanism for cloud
656 condensation nuclei in the remote marine boundary layer, J. Geophys. Res.-Atmos., 100,
657 2893–2903, https://doi.org/10.1029/94jd02832, 1995.
658 Rienecker, M. M., Suarez, M. J., Gelaro, R., Todling, R., Bacmeister, J., Liu, E., Bosilovich, M.
659 G., Schubert, S. D., Takacs, L., Kim, G.-K., Bloom, S., Chen, J., Collins, D., Conaty, A.,
660 da Silva, A., Gu, W., Joiner, J., Koster, R. D., Lucchesi, R., … Woollen, J. (2011).
661 Merra: NASA's modern-era retrospective analysis for research and applications. *Journal*
662 *of Climate*, *24*(14), 3624–3648. https://doi.org/10.1175/jcli-d-11-00015.1
663 Russell, L. M., Pandis, S. N., and Seinfeld, J. H.: Aerosol production and growth in the marine
664 boundary layer, J. Geophys. Res.-Atmos., 99, 20989–21003,
665 https://doi.org/10.1029/94jd01932, 1994.
666 Shaw, G. E. (1988). Antarctic Aerosols: A Review. *Reviews of Geophysics*, *26*(1), 89–112.
667 https://doi.org/10.1029/rg026i001p00089
668 Simmons, J. B., Humphries, R. S., Wilson, S. R., Chambers, S. D., Williams, A. G., Griffiths, A.
669 D., McRobert, I. M., Ward, J. P., Keywood, M. D., & Gribben, S. (2021). Summer
670 aerosol measurements over the East Antarctic Seasonal Ice Zone. *Atmospheric Chemistry*
671 *and Physics*, *21*(12), 9497–9513. https://doi.org/10.5194/acp-21-9497-2021
672 Stein, A. F., Draxler, R. R., Rolph, G. D., Stunder, B. J., Cohen, M. D., & Ngan, F. (2015).
673 NOAA's Hysplit Atmospheric Transport and dispersion modeling system. *Bulletin of the*

American Meteorological Society, *96*(12), 2059–2077. https://doi.org/10.1175/bams-d-14-00110.1

Terai, C. R., Klein, S. A., & Zelinka, M. D. (2016). Constraining the low-cloud optical depth feedback at middle and high latitudes using satellite observations. *Journal of Geophysical Research: Atmospheres*, *121*(16), 9696–9716. https://doi.org/10.1002/2016jd025233

Tiszenkel, L., Stangl, C., Krasnomowitz, J., Ouyang, Q., Yu, H., Apsokardu, M. J., Johnston, M. V., & Lee, S.-H. (2019). Temperature effects on sulfuric acid aerosol nucleation and growth: Initial results from the tangent study. *Atmospheric Chemistry and Physics*, *19*(13), 8915–8929. https://doi.org/10.5194/acp-19-8915-2019

, C. H., DeMott, P. J., Russell, L. M., Toohey, D. W., Rainwater, B., Geiss, R., Sanchez, K. J., Lewis, S., Roberts, G. C., Humphries, R. S., McCluskey, C. S., Moore, K. A., Selleck, P. W., Keywood, M. D., Ward, J. P., & McRobert, I. M. (2021). Cloud-nucleating particles over the Southern Ocean in a changing climate. *Earth's Future*, *9*(3). https://doi.org/10.1029/2020ef001673

Zelinka, M. D., Myers, T. A., McCoy, D. T., Po-Chedley, S., Caldwell, P. M., Ceppi, P., Klein, S. A., & Taylor, K. E. (2020). Causes of higher climate sensitivity in CMIP6 models. *Geophysical Research Letters*, *47*(1). https://doi.org/10.1029/2019gl085782